

Silicon spin chains at finite temperature: dynamics of Si(553)-Au

Steven C. Erwin*

Center for Computational Materials Science, Naval Research Laboratory, Washington, DC 20375

P.C. Snijders

Materials Science and Technology Division, Oak Ridge National Laboratory, Oak Ridge, TN 37830

(Dated: July 5, 2018)

When gold is deposited on Si(553), the surface self-assembles to form a periodic array of steps with nearly perfect structural order. In scanning tunneling microscopy these steps resemble quasi-one-dimensional atomic chains. At temperatures below ~ 50 K the chains develop a tripled periodicity. We recently predicted, on the basis of density-functional theory calculations at $T = 0$, that this tripled periodicity arises from the complete polarization of the electron spin on every third silicon atom along the step; in the ground state these linear chains of silicon spins are antiferromagnetically ordered. Here we explore, using ab-initio molecular dynamics and kinetic Monte Carlo simulations, the behavior of silicon spin chains on Si(553)-Au at finite temperature. Thermodynamic phase transitions at $T > 0$ in one-dimensional systems are prohibited by the Mermin-Wagner theorem. Nevertheless we find that a surprisingly sharp onset occurs upon cooling—at about 30 K for perfect surfaces and at higher temperature for surfaces with defects—to a well-ordered phase with tripled periodicity, in good agreement with experiment.

I. INTRODUCTION

Linear atomic chains of metal atoms on semiconductor surfaces offer, in principle, the physical realization of phenomena predicted theoretically for one-dimensional model systems. In practice, however, unanticipated interactions can often complicate the picture and lead to behavior not easily explained by simple models. In this article we demonstrate theoretically how the complex interactions among polarized electron spins in silicon surface states determine the observed behavior of a well-studied atomic chain system, Si(553)-Au, over a wide range of temperatures. The methods developed here and the resulting predictions—which are qualitatively and quantitatively consistent with experimental observations—are also likely to apply more broadly to other vicinal Si/Au chain systems, such as Si(557)-Au.

The Si(553)-Au surface was first investigated in Ref. 1, an experimental study which established that the electronic band dispersion and fermi surface were indeed those of a nearly one-dimensional metal. Since then, numerous lines of research have emerged. Efforts to determine the basic atomic structure of the surface have been based on data from diffraction experiments^{2–4} and on the results of theoretical total-energy calculations.^{5–8} These were greatly aided by the first definitive determination of the coverage of Au atoms on Si(553)-Au.⁹ Other investigations have explored the properties of finite-length chains^{10,11} as well as various native defects¹² and foreign adsorbates^{13–19} on the nominally clean Si(553)-Au surface.

One particularly interesting line of research has focused on the collective behavior in Si(553)-Au that emerges at low temperature. Ideal one-dimensional metals with partially filled bands exhibit a broken symmetry at low temperature, namely a charge-density wave arising from the Peierls instability. Indeed, broken symmetries in

Si(553)-Au were observed using scanning tunneling microscopy (STM) in Refs. 20 and 21. Images acquired at room temperature showed alternating bright and dim rows with unit periodicity a_0 along the rows. Below ~ 50 K these rows separately developed higher-order periodicity: a tripled period ($3a_0$) along the bright rows and a doubled period ($2a_0$) along the dim rows. Subsequent review articles have discussed possible explanations for these observations.^{22,23}

Notwithstanding the fact that Peierls instabilities lead to higher-order periodicity, a completely different theoretical explanation for the coexisting triple and double periodicities in Si(553)-Au was proposed in Ref. 24. The key idea, which was based on the results of density-functional theory (DFT) calculations, was that the ground state of Si(553)-Au is spin polarized. In the DFT ground state, the silicon atoms that comprise the steps on this vicinal surface have dangling bonds, every third of which is occupied by a single fully polarized electron while the other two are doubly occupied. The bright rows seen in empty-state STM images arise from these step-edge silicon atoms. At low temperature the $3a_0$ peaks that appear in this row are from the spin-polarized atoms, which have precisely this periodicity. The DFT ground state also reveals a period doubling within the row of Au atoms. Both of these higher-order periodicities disappear if spin polarization is suppressed in the calculation, providing compelling evidence that spin polarization is the primary mechanism underlying the observed symmetry breaking in Si(553)-Au.

Experiments were subsequently carried out to look for a spectroscopic signature of this predicted spin-polarized ground state. The DFT calculations showed that an unoccupied state should exist 0.5 eV above the fermi level and be localized at the polarized silicon atoms.²⁴ The existence and spectral and spatial location of this state was indeed confirmed by two-photon photoemission²⁵ and by

scanning tunneling spectroscopy.²⁶

The predictions of Ref. 24 only addressed the zero-temperature ground state of Si(553)-Au. Left unanswered in that work was the question of how the broken-symmetry ground state evolves to have normal a_0 periodicity above ~ 50 K. This article addresses that question from a theoretical and computational perspective. Although it may seem obvious that thermal fluctuations are important, the nature of these fluctuations turns out to be unexpectedly subtle. Nevertheless, we derive here a number of detailed qualitative as well as quantitative predictions that can easily be tested experimentally. The results of these tests will furnish additional evidence for evaluating the validity of the basic mechanism proposed in Ref. 24.

II. GROUND STATE CONFIGURATION

The physical and magnetic structure of Si(553)-Au in its ground state were first proposed and discussed in Ref. 24 and for reference are reproduced in Fig. 1. This is a stepped surface consisting of (111) terraces and bilayer steps, and is stabilized by Au atoms that substitute for Si atoms in the surface layer of the terrace. The steps themselves consist of Si atoms organized into a thin graphitic strip of honeycomb hexagons (the green atoms in Fig. 1).

The surface electronic structure of Si(553)-Au has two main contributions. The first consists of two intense quasi-1D parabolic electron bands centered at the boundary of the surface Brillouin zone. These “Au bands” arise from the bonding and antibonding combinations of Au 6s and subsurface Si orbitals (purple atoms). The bonding Au band is approximately half-filled and the antibonding band approximately one-fourth filled.

The second contribution arises from the very edge of the Si honeycomb chain, which consists of threefold-coordinated Si atoms. The unpassivated sp^3 orbitals of these atoms can in principle be occupied by zero, one, or two electrons. The Si atoms themselves supply, on average, one electron per orbital. The step edge does not necessarily maintain this average occupancy, because electronic charge can also be transferred to or from the Au bands. Indeed, DFT calculations predict that the lowest energy configuration has one electron in every third orbital (red and blue atoms in Fig. 1) and double occupancy everywhere else (green atoms). The singly occupied orbitals are completely spin-polarized and hence have local spin moments of 1 bohr magneton each. Physically, these atoms relax slightly downward, by 0.3 \AA , compared to their nonpolarized neighbors. The sign of the spins alternates along the step edge, with antiferromagnetic order favored by 15 meV per spin relative to ferromagnetic order. Therefore the magnetic periodicity is $6a_0$, where a_0 is the Si surface lattice constant. This is also the smallest period that allows for the coexistence of $3a_0$ spacing of the spins and $2a_0$ spacing (period doubling) within the Au chain. This coexistence was first observed

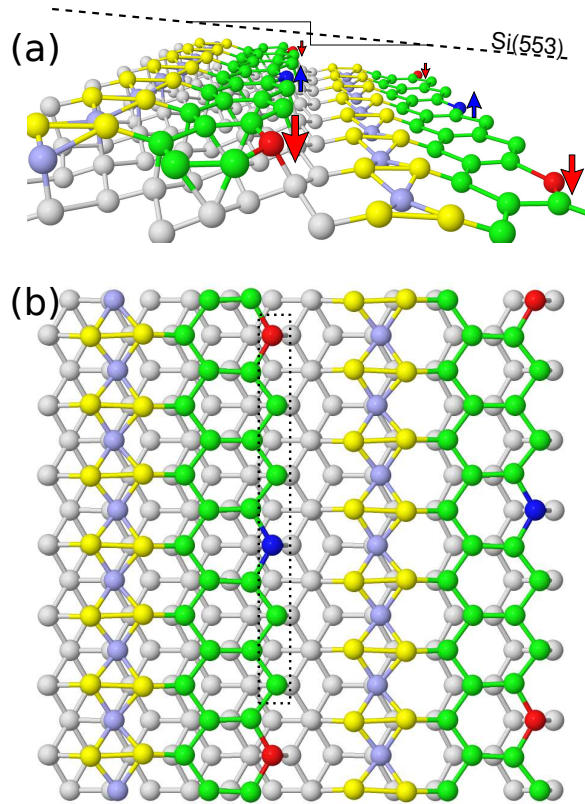


FIG. 1. (Color online) (a,b) Perspective and top views of Si(553)-Au in its electronic ground state. Yellow atoms are Au, all others are Si. The Au atoms are embedded in flat terraces, which are separated by steps consisting of Si atoms arranged as a honeycomb chain (green). Every third Si atom (red, blue) at the step has a spin magnetic moment of one Bohr magneton ($S = 1/2$, arrows) from the complete polarization of the electron occupying the dangling-bond orbital. The sign of the polarization (red vs. blue) alternates along the step. The six atoms in the outlined box are the focus of the ab-initio molecular dynamics discussed in Sec. III.

in STM experiments^{20,21} and emerges naturally in DFT calculations—but only when the spin degree of freedom is unconstrained.²⁴

III. FINITE TEMPERATURE DYNAMICS

The remainder of this article explores excitations of Si(553)-Au from its ground state due to finite temperature. Two main theoretical tools were used: ab-initio molecular dynamics (MD) and kinetic Monte Carlo (kMC) simulations. The first was used to identify the most important low-energy activated processes and to determine their activation barriers. Because of the complexity of the system only small time scales (tens of ps) and a small (1×6) simulation cell could be ad-

dressed using ab-initio MD. To reach much longer time scales (tens of ns) and larger system sizes (up to 128 spins) we constructed a one-dimensional kMC model based on the processes and barriers determined from ab-initio MD. In particular, the kMC model allowed us to investigate finite-temperature behavior in the presence of pinning defects—providing useful insight into temperature-dependent results from scanning probe experiments, where defects often play a critical role.

Two simplifying assumptions were used throughout this work. (1) Electronic excitations were not considered, and consequently the system stays on the Born-Oppenheimer surface. This assumption is reasonable in view of the modest temperatures—room temperature and lower—considered here. (2) Spin flips were not allowed. Although, as we will see below, the spins can diffuse among the Si step-edge atoms, their signs and ordering remained that of the original antiferromagnetic ordering. Although a different initial spin ordering might affect some details of the simulation, the overall qualitative findings would be very similar.

A. Ab-initio molecular dynamics

The MD simulations were performed using the same basic geometry and computational parameters described in Ref. 24. The Si(553)-Au surface was represented by six layers of Si plus the reconstructed top surface layer and a vacuum region of 10 Å. All atoms were free to move during the simulation except the bottom Si layer and its passivating hydrogen layer. Total energies and forces were calculated within the generalized-gradient approximation of Perdew, Burke, and Ernzerhof to DFT using projector-augmented wave potentials, as implemented in VASP.^{27–30} The plane-wave cutoff was 200 eV and only the Γ point was used. The dynamics simulations were performed in the canonical ensemble using a Nosé thermostat and a time step of 3 fs. Five temperatures, equally spaced in $1/T$, were used (57, 67, 80, 110, 133 K). For each temperature a thermalization run of 10 ps was first performed, followed by a dynamics run of 20 ps.

Figure 2 shows the resulting atomic trajectories during the entire run of 10^4 MD time steps for the lowest temperature studied, 57 K. The six curves are for the six Si step-edge atoms in the outlined box of Fig. 1(b). The upper and lower panels show the relative heights of the atoms and their local spin moments, respectively. After thermalization was achieved the system settled into its ground state configuration with two spin-polarized atoms (red and blue) sitting ~ 0.3 Å lower than their four non-polarized neighbors.

The expanded view in Fig. 2(b) focuses on two events that occurred between 15 and 16 ps. At 15.44 ps the magnitude of the moment on the spin-up red atom went rapidly to zero while, concurrently, a spin-up moment rapidly developed on the neighboring cyan atom. At essentially the same time the height of the red atom in-

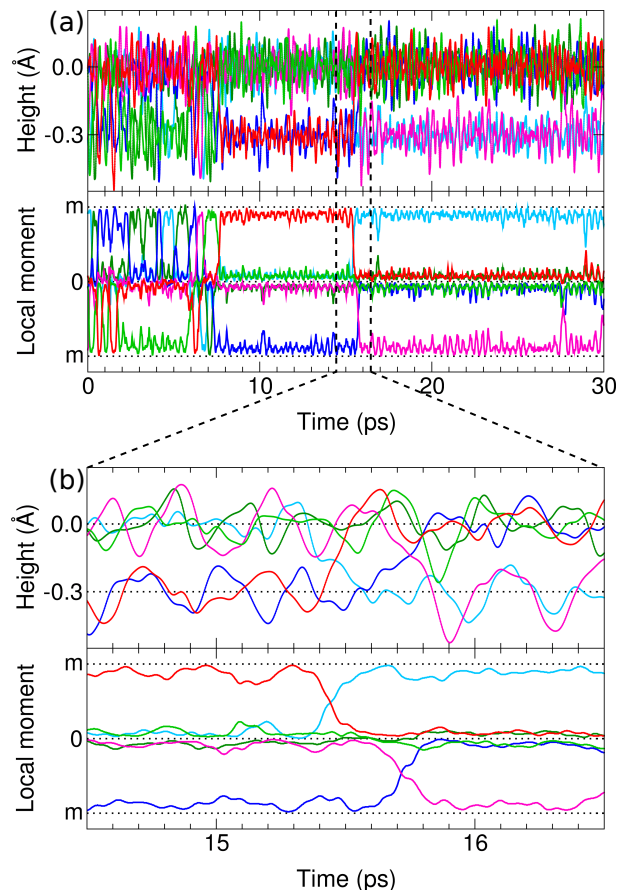


FIG. 2. (Color online) (a) Ab-initio molecular dynamics trajectories of the six Si step-edge atoms outlined in Fig. 1, at 57 K. Red and blue curves denote the red and blue atoms, which are initially spin-polarized. Other colors (magenta, cyan, dark green, light green) denote initially non-polarized atoms. Thermalization is completed by about 10 ps. Upper panel: height of each atom, relative to the average height of nonpolarized atoms. Lower panel: local spin moment of each atom. (b) Expanded view of two spin hops occurring at 15.44 ps (from the red atom to the cyan atom) and at 15.71 ps (from the blue atom to the magenta atom).

creased by 0.3 Å to that of a non-polarized atom, while the cyan atom moved down by the same amount. In summary, the spin-up moment that was localized on the red atom hopped to one of its neighbors.

Very soon after, a second hop occurred at 15.71 ps. This hop was made by the other spin (with the opposite sign) which moved from the blue atom to the magenta atom. It is not a coincidence that this hop occurred so soon after the first. The first hop changed the minimum spacing between spins from $3a_0$ to $2a_0$, incurring an energy penalty (discussed in detail below). This increase in energy in turn reduced the barrier for any hop that restores the spacing to its optimal value. The cyan and magenta atoms are indeed separated by $3a_0$, and thus after two rapid spin hops the system was restored to an equivalent ground state configuration, in which it

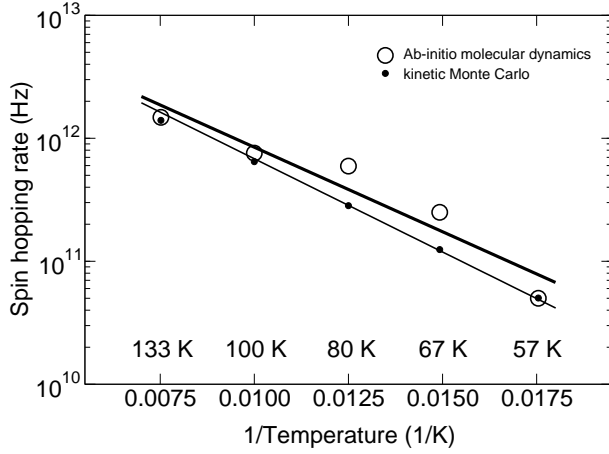


FIG. 3. Temperature dependence of the hopping rate for Si spins along the Si(553)-Au step edge. The rates are time averages extracted from ab-initio molecular dynamics (MD) trajectories, and are compared to rates from kinetic Monte Carlo (kMC) simulations. The linear fits describe Arrhenius behavior. The fit to ab-initio MD rates (thick line) gives a pre-exponential factor $2.0 \times 10^{13} \text{ s}^{-1}$ and activation barrier 12 meV. For kMC rates (thin line) the values are $2.2 \times 10^{13} \text{ s}^{-1}$ and 13 meV.

remained for the rest of the simulation.

The very small number of hops observed at 57 K makes it clear that ab-initio MD simulations of Si(553)-Au at still lower temperatures, where many of the relevant experiments are conducted, are not feasible. Instead we turn to higher temperatures and ask how the frequency of hopping events depends on temperature. This information will be useful in Sec. III B for calibrating and validating our kMC model in a temperature range accessible to both methods.

Figure 3 shows the resulting time-averaged hopping rate for a single spin, versus inverse temperature. The rates for low temperatures have large statistical uncertainties (not shown) and hence it is reasonable to describe these results by a simple linear Arrhenius fit, as shown. The attempt frequency, $2.0 \times 10^{13} \text{ s}^{-1}$, is on the order of a surface vibrational frequency, as expected. The activation energy, 12 meV, represents a characteristic average of the individual barriers for spin hops weighted by their relative probability of occurrence.

B. Kinetic Monte Carlo model

To construct the kMC model one first needs to enumerate all the relevant spin hops and their individual rates. We used DFT results obtained from the full Si(553)-Au system for this task. In the spirit of simplicity we constructed the kMC model itself to be strictly one-dimensional, with an arbitrarily large unit cell and periodic boundary conditions. Thus the kMC simulations inherit much of the accuracy of the DFT calculations but

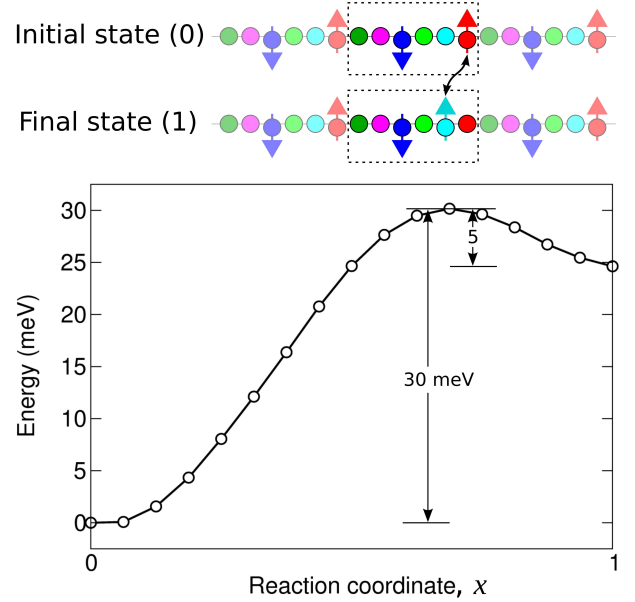


FIG. 4. DFT potential energy surface for a single spin hopping from the red atom to the neighboring cyan atom. The initial state (0) is the ground state depicted in Fig. 1. The final state (1) is the metastable state, fully relaxed, that exists between 15.44 and 15.71 ps in the MD simulation of Fig. 2. The activation barrier is 30 meV for the forward reaction and 5 meV for the reverse reaction. Atom colors correspond to the trajectories in Fig. 2.

make the additional approximation that spin hops along different step edges are independent.

Figure 4 shows the DFT potential energy surface for the spin hop observed in Fig. 2(b) at 15.44 ps into the MD simulation. Because the spins and the heights of the atoms are tightly linked, the reaction coordinate x is approximately given by the relative heights h of the red and cyan atoms,

$$x \approx [1 - (h_{\text{cyan}} - h_{\text{red}})/\Delta h]/2, \quad (1)$$

where $\Delta h = 0.3 \text{ \AA}$ is the equilibrium height difference between spin-polarized and non-polarized atoms. To definitively determine the detailed reaction pathway and potential energy surface we used the nudged elastic-band method.

This potential energy surface confirms the assertion, made in Sec. III A, that the red-to-cyan (forward) spin hop incurs an energy penalty that leads to a smaller barrier for the cyan-to-red (reverse) hop. Specifically, the activation barrier for the forward hop is 30 meV, the resulting energy penalty is 25 meV, and the barrier for the reverse hop is 5 meV. These two types of hops, and their calculated barriers, are two of the three fundamental processes included in our kMC model.

For convenience we define here a more compact notation for enumerating the different types of spin hops. Careful examination of the ab-initio MD trajectories reveals that all spin hops were to an adjacent site; there

were no double hops. Hence we can label every hop as either leftward (\leftarrow) or rightward (\rightarrow). We assume that the barrier for a spin hop depends only on the spin's immediate environment, that is, on the distances ma_0 and na_0 to the left and right neighboring spins, respectively, measured before making the hop. Using this notation we can express the barriers for the two hops shown in Fig. 4 as $b(3, 3, \leftarrow) = 30$ meV and $b(2, 4, \rightarrow) = 5$ meV, where the two numerical arguments denote m and n , respectively.

The third important hop we considered occurs when $m + n = 5$, rather than 6 as depicted in Fig. 4. From DFT nudged elastic-band calculations we find $b(3, 2, \leftarrow) = b(2, 3, \rightarrow) = 14$ meV (the barriers are equal by symmetry). As expected from the distances to the neighboring spins, this barrier is in between the previous two.

The MD trajectories also show that two spins never occupy adjacent sites. Because of this, our enumeration of the possible spin hops is already complete for all cases with $m+n \leq 6$. (It is worth noting that the configuration in which a spin has both neighbors at $2a_0$ is allowed, but because its adjacent sites cannot be occupied this spin cannot hop until one of its neighbors does.) The cases with $m+n \geq 7$ are difficult to treat within DFT but occur more rarely and thus are less important. For this reason we treated the effect of neighbors beyond $3a_0$ as negligible, used the barrier of 30 meV for any hop that brings a spin within $2a_0$ of its neighbor, and assigned a single (arbitrary) barrier of 10 meV to hops that maintain larger separations than this. This completes our enumeration.

To finish the construction of the kMC model, we assumed that the rates for all allowed spin hops are given by $r = a \exp(-b/kT)$, where a is a common prefactor and $b = b(m, n, \leftarrow)$ and $b(m, n, \rightarrow)$ are the DFT barriers.

To determine the optimal value of a and compare the predictions of the kMC model to the ab-initio MD results, we applied the model to the system discussed in Sec. III A—two spin-polarized atoms in a six-atom unit cell with periodic boundary conditions. The resulting kMC spin hopping rates obtained using $a = 6 \times 10^{12} \text{ s}^{-1}$ are plotted in Fig. 3 for direct comparison with the rates from ab-initio MD. The kMC rates have negligible statistical errors and it is clear that a simple Arrhenius fit describes them very well. Moreover, the fitted attempt frequency, $2.2 \times 10^{13} \text{ s}^{-1}$, and activation energy, 12 meV, are within 10% of the MD values. This confirms that the kMC model accurately reproduces the ab-initio results within the temperature range considered.

C. Spins at finite temperature near a defect

In real systems, the behavior of collective phenomena is often controlled by defects that pin the phase of a low-temperature state having broken symmetry. On the Si(553)-Au surface, a variety of defects—missing atoms, adsorbates, etc.—have been observed to act as pinning sites that locally stabilize the 1×3 ground state.^{17,21,23,31} The important role played by such pinning defects moti-

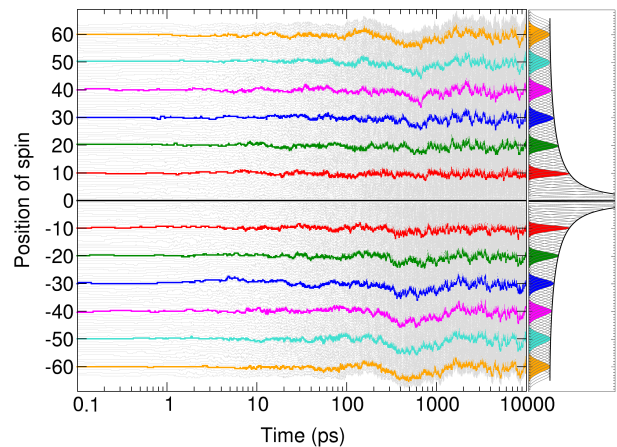


FIG. 5. (Color online) Kinetic Monte Carlo trajectories of 128 spins at 300 K in the presence of a pinning defect at the origin. Every tenth trace is colored for clarity. Right panel: histogram of the positions occupied by each spin, weighted by the time spent there, obtained over a simulation time of $1 \mu\text{s}$. The heavy curve is the envelope function $d^{-2/3}$ describing the decay of histogram heights with distance d from the pinning defect.

vates our first application of the kMC model.

We prepared a system consisting of 128 independent spins, with periodic boundary conditions, initially arranged in the antiferromagnetic ground state with uniform $3a_0$ spacing. One of the spins (at position 0) was pinned in place throughout the simulation, thus representing a generic immobile defect. The spins were allowed to hop stochastically among the 3×128 lattice sites according to probabilities defined by the hopping rates r .

Figure 5 displays the resulting trajectories at 300 K of all the spins over the first 10 ns of the simulation. For clarity every tenth trajectory trace is colored. As the system evolved, each spin explored a region of the lattice around its initial position. These explorations were relatively small for spins near the pinning defect and became progressively larger for spins farther away.

The right panel in Fig. 5 examines this thermally induced wandering in greater detail. For each of the 128 spins a histogram was made representing the position of that spin at 300 K. At this temperature a simulation time of $1 \mu\text{s}$ was sufficient to obtain the steady-state distribution. It is readily apparent from examining the colored histograms that each is well described by a gaussian function centered on the spin's initial position. Thus each of these gaussians is entirely specified by its variance σ^2 , whose value depends on the distance d to the pinning defect. To deduce this dependence we first note that the area under each gaussian is by construction the same. Hence the height of each gaussian is proportional to $1/\sigma$. We find empirically that the dependence of these heights on distance is given with excellent accuracy as $d^{-2/3}$. An envelope function with this dependence is shown on the histogram plot as a heavy black curve. From this depen-

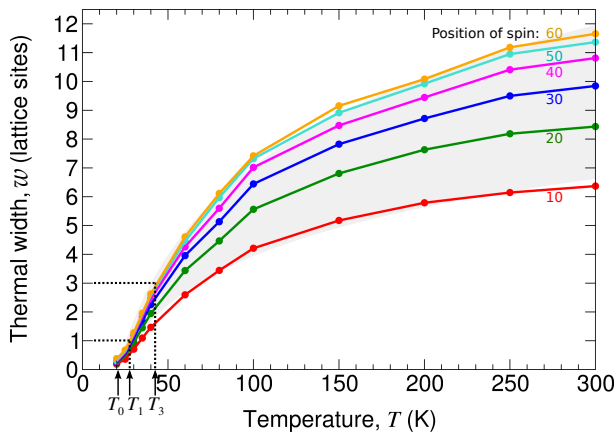


FIG. 6. (Color online) Temperature dependence of the thermal widths $w(T)$ of every tenth spin, in the presence of a pinning defect. Labels indicate the spin's distance from the defect, in units of $3a_0$. Colors correspond to the trajectories in Fig. 5. The light gray shaded area is bounded by logarithmic fits to the lower (red) and upper (orange) data points. The characteristic temperatures T_0 , T_1 , and T_3 describe different criteria by which thermal wandering of spins is expected to be either eliminated or suppressed; see discussion in text.

dence we thus deduce that the thermally induced widths w , defined here as 2σ , increase with distance from a pinning defect as $w \sim d^{2/3}$.

Now we move on to explore how temperature affects the thermal wandering of spins near a pinning defect. We repeated the kMC simulation and analysis in Fig. 5 for a series of temperatures between 10 and 300 K. We focus on the variation of the thermal widths w as a function of temperature T .

Figure 6 summarizes the resulting temperature dependence. The six datasets show $w(T)$ for every tenth spin of the 128-spin simulation cell. For reference, the six values at $T = 300$ K correspond to the six gaussian widths in the upper half of the histogram panel in Fig. 5. We find empirically that the dependence of each dataset on temperature is close to logarithmic, as shown by the light gray shaded area. This implies that the dependence of the thermal widths on distance and temperature can be separated and written as

$$w(d, T) = w_0(d) \ln(T/T_0), \quad (2)$$

where $w_0(d) \sim d^{2/3}$ and the characteristic temperature T_0 has the fitted value 21 K. All thermal wandering is, by definition, completely eliminated at T_0 . But two less restrictive criteria may be more relevant for interpreting the experimentally observed transition to the period-tripled ground state. At $T_1 = 27$ K the thermal widths for all 128 spins become smaller than the width of a single lattice site. Hence, below this temperature the spins will in effect be frozen into place on every third lattice site. At still higher temperature, $T_3 = 42$ K, all thermal widths are less than or equal to the average spacing (three lattice sites) between spins. Hence the spins will

first become distinguishable as the system is cooled below this temperature.

To generalize this result and make predictions that can be tested by experiment, we first assume that real systems can be characterized by a known average concentration c of pinning defects. Because the defects are distributed in 1D, the characteristic distance d from a spin to the nearest defect scales as $1/c$. By inverting Eq. 2 we then immediately obtain a simple result: the temperatures $T_{1,3}$ at which all spins in the system become either frozen into place or distinguishable will scale as $T_{1,3} \sim \exp(c^{2/3})$. Thus we predict this scaling to describe the temperature at which the period-tripled ground state of Si(553)-Au is first observed.

By inserting into this qualitative relationship the appropriate constants obtained from the kMC simulations, we derive a quantitative prediction for the freezing temperature,

$$T_1 = T_0 \exp(k c^{2/3}), \quad (3)$$

where $k = 11.8$ is a dimensionless constant and c is expressed in the dimensionless units of defects per lattice site. The corresponding equation for T_3 can be obtained from Eq. 3 by multiplying the argument of the exponential by three. A useful guide to understanding the importance of defects in Si(553)-Au is provided by linearizing Eq. 3 around a physically plausible value (10^{-2}) for the defect concentration. This leads to the result that a change in the defect concentration will raise the freezing temperature by $\Delta T_1 = \gamma \Delta c$, with proportionality constant $\gamma = 1330$ K. Thus, for samples with approximately one defect every 100 lattice sites, a doubling of this concentration will increase the freezing temperature by 13 K.

D. Spins at finite temperature in the absence of defects

Although a system completely free of defects is obviously unrealistic, the behavior of such an idealized system nevertheless offers complementary insight into the thermal wandering of spins when the concentration of defects is very low. As we show below, despite the absence of defects, the statistical behavior of the spins still exhibits a sudden and qualitative change at about 30 K.

We constructed a periodic system of 64 spins similar to that described in Sec. III C, but now without a pinning defect. Thus each spin executed a random walk in 1D. Figure 7 shows a typical trajectory at 100 K for one of the 64 spins. Despite the stochastic nature of this single trajectory, it is already plausible that the average displacement $\langle d \rangle$ depends on the time t according to $\langle d \rangle \propto \sqrt{t}$, which is the well-known result for a single unbiased random walker in one dimension.

To analyze this behavior more systematically, we performed many independent kMC simulations and computed the average displacements as a function of time.

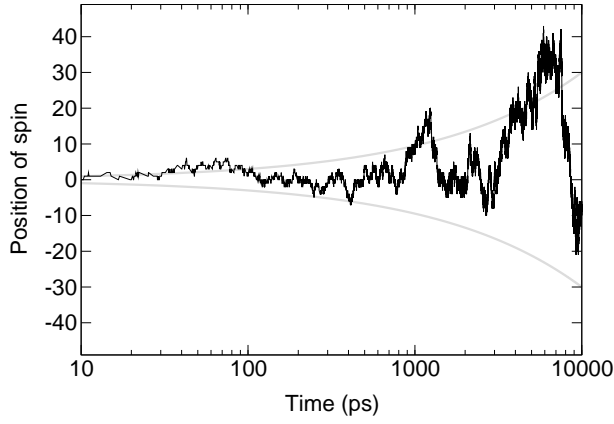


FIG. 7. Trajectory of a single spin at 100 K in the absence of pinning defects. Gray curve shows the theoretical average displacement versus time for a isolated random walker in one dimension, $\langle d \rangle \propto \sqrt{t}$.

Figure 8 shows these averages on a log-log scale for a range of temperatures. At high temperatures we indeed obtain the behavior $\langle d \rangle \propto t^{1/2}$, which is indicated by the dotted line. This behavior persists until the temperature reaches the range 30–35 K, where it still exhibits power-law behavior $\langle d \rangle \propto t^H$ but with a progressively larger exponent $H > 1/2$.

In general, a system for which the long-time displacements are characterized by a Hurst exponent $H = 1/2$ is said to be uncorrelated, while $H > 1/2$ indicates that

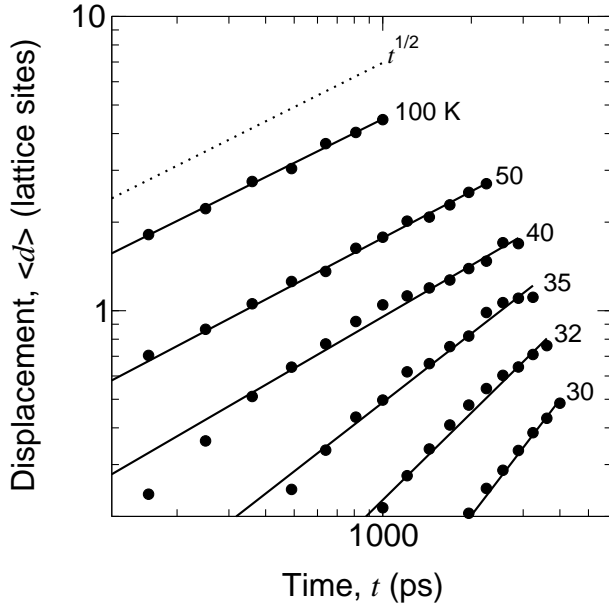


FIG. 8. Average displacement versus time of a single spin in the absence of defects, at the indicated temperatures. Circles are statistical averages over 2000 kMC simulations. Straight lines are fits to t^H , where H is the Hurst exponent. The dotted line indicates $H=1/2$.

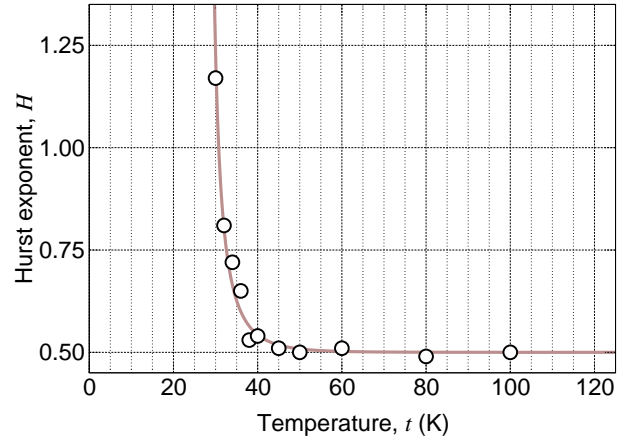


FIG. 9. Hurst exponent versus temperature for spins in the absence of a defect. The solid curve is a fit to a generalized susceptibility with a characteristic temperature $T_c = 28$ K.

long-time correlations are present.³² Figure 9 shows the Hurst exponent H , obtained by fitting the time-averaged displacements, as a function of temperature. Above ~ 40 K the system displays uncorrelated behavior. Below this temperature we observe the rapid onset of correlated behavior. To quantify the temperature of this transition we fit the Hurst exponents to a generalized susceptibility of the form $H = (1/2)/[1 - (T_c/T)^\nu]$ and obtain a characteristic temperature $T_c = 28$ K. Hence as the clean system is cooled toward T_c the random walks described by individual spins rapidly lose their independent character. This transition occurs with a characteristic temperature comparable to that obtained, $T_0 = 21$ K, by extrapolating from the behavior in the presence of defects. Thus these two complementary approaches lead to qualitatively as well as quantitatively similar conclusions.

IV. DISCUSSION AND CONCLUSIONS

A guiding principle in one-dimensional physics is provided by the Mermin-Wagner theorem, which states that phase transitions cannot occur above $T = 0$ if the interactions are short-ranged.³³ Exploring the different manifestations of this theorem in real systems can yield new and unanticipated insights. For example, a previous publication by one of us demonstrated theoretically that when the interactions are *not* short-ranged, as for $1/r$ Coulomb interactions, then a well-defined thermodynamic phase transition can indeed occur—and likely does occur for a system of Ba adsorbates on Si(111).^{34,35} In the present article the new insights into 1D physics are of a different kind: we have shown that even when the interactions are short-ranged, and the system purely 1D, a well-ordered phase with the clear signature of a broken symmetry can form well above $T = 0$. Moreover, an approximate transition temperature can be readily identified using realistic simulations and straightforward statistical analysis.

For Si(553)-Au the precise nature of the interacting entities is unexpected and somewhat subtle: our MD simulations showed that they are neither simple vibrations of atoms, nor spins on a simple fixed lattice, but rather a tightly coupled combination of both. In this sense a description of Si(553)-Au based on spin polarons is appropriate. Our kMC simulations showed that as the temperature of the system is raised, the ground state $3a_0$ crystal formed by these polarons melts at a temperature we estimate to be ~ 30 K for perfectly clean systems, and higher for systems with pinning defects. A direct experimental test of this description is afforded by Eq. 3, which predicts how the transition temperature varies with the concentration of defects.

It is important to acknowledge some limitations of this work. Because our focus has been on the behavior of Si(553)-Au at low temperature, we have assumed that the spin-polarized silicon states remain polarized at higher temperatures. Our preliminary calculations indicate that this assumption is completely justified at the temperatures of interest here. However, at much higher temperatures the thermally induced vibrations of the step edge atoms increasingly render the system nonpolarized for part of the time. For example, at room temperature the average spin moment is reduced to roughly $2/3$ of its

low-temperature value of 1 bohr magneton. Future theoretical investigations into the behavior of Si(553)-Au near room temperature will have to account for this thermal suppression of the spin polarization.

Finally, as mentioned in Sec. III, we have throughout assumed for simplicity that the ordering of the spins remains antiferromagnetic, as in the ground state. Preliminary calculations show that the barriers for spin hopping depend quantitatively, although not qualitatively, on the signs of the neighboring spins. A generalization of our kMC model that includes spin flips would be a very interesting direction to pursue, but we anticipate that the qualitative conclusions drawn here—as well as the overall consistency between our findings and those of existing experiments—would be largely unchanged.

ACKNOWLEDGMENTS

Many discussions with F.J. Himpsel are gratefully acknowledged. This work was supported by the Office of Naval Research (SCE) and the Department of Energy, Basic Energy Sciences, Materials Sciences and Engineering Division (PCS). Computations were performed at the DoD Major Shared Resource Centers at AFRL and ERDC.

-
- * steve.erwin@nrl.navy.mil
- ¹ J. N. Crain, A. Kirakosian, K. N. Altmann, C. Bromberger, S. C. Erwin, J. McChesney, J.-L. Lin, and F. J. Himpsel, *Phys. Rev. Lett.* **90**, 176805 (2003).
 - ² S. K. Ghose, I. K. Robinson, P. A. Bennett, and F. J. Himpsel, *Surf. Sci.* **581**, 199 (2005).
 - ³ T. Takayama, W. Voegeli, T. Shirasawa, K. Kubo, M. Abe, T. Takahashi, K. Akimoto, and H. Sugiyama, *e-Journal of Surface Science and Nanotechnology* **7**, 533 (2009).
 - ⁴ W. Voegeli, T. Takayama, T. Shirasawa, M. Abe, K. Kubo, T. Takahashi, K. Akimoto, and H. Sugiyama, *Physical Review B* **82**, 075426 (2010).
 - ⁵ S. Riikonen and D. Sanchez-Portal, *Nanotechnology* **16**, S218 (2005).
 - ⁶ S. Riikonen and D. Sanchez-Portal, *Surf. Sci.* **600**, 1201 (2006).
 - ⁷ S. Riikonen and D. Sanchez-Portal, *Physical Review B* **77**, 165418 (2008).
 - ⁸ M. Krawiec, *Physical Review B* **81**, 115436 (2010).
 - ⁹ I. Barke, F. Zheng, S. Bockenhauer, K. Sell, V. v. Oeynhausen, K. H. Meiwes-Broer, S. C. Erwin, and F. J. Himpsel, *Physical Review B* **79**, 155301 (2009).
 - ¹⁰ J. N. Crain and D. T. Pierce, *Science* **307**, 703 (2005).
 - ¹¹ J. N. Crain, M. D. Stiles, J. A. Stroscio, and D. T. Pierce, *Phys. Rev. Lett.* **96**, 156801 (2006).
 - ¹² H. Okino, I. Matsuda, S. Yamazaki, R. Hobara, and S. Hasegawa, *Physical Review B* **76**, 035424 (2007).
 - ¹³ K.-D. Ryang, P. G. Kang, H. W. Yeom, and S. Jeong, *Physical Review B* **76**, 205325 (2007).
 - ¹⁴ H. Okino, I. Matsuda, R. Hobara, S. Hasegawa, Y. Kim, and G. Lee, *Physical Review B* **76**, 195418 (2007).
 - ¹⁵ J. R. Ahn, P. G. Kang, J. H. Byun, and H. W. Yeom, *Physical Review B* **77**, 035401 (2008).
 - ¹⁶ P.-G. Kang, H. Jeong, and H. W. Yeom, *Physical Review B* **79**, 113403 (2009).
 - ¹⁷ P.-G. Kang, J. S. Shin, and H. W. Yeom, *Surf. Sci.* **603**, 2588 (2009).
 - ¹⁸ P. Nita, M. Jalochofski, M. Krawiec, and A. Stepniak, *Phys. Rev. Lett.* **107**, 026101 (2011).
 - ¹⁹ M. Krawiec and M. Jalochofski, *Physical Review B* **87**, 5445 (2013).
 - ²⁰ J. R. Ahn, P. G. Kang, K. D. Ryang, and H. W. Yeom, *Phys. Rev. Lett.* **95**, 196402 (2005).
 - ²¹ P. C. Snijders, S. Rogge, and H. H. Weitering, *Phys. Rev. Lett.* **96**, 076801 (2006).
 - ²² P. C. Snijders and H. H. Weitering, *Reviews of Modern Physics* **82**, 307 (2010).
 - ²³ S. Hasegawa, *J. Phys.: Condens. Matter* **22**, 084026 (2010).
 - ²⁴ S. C. Erwin and F. J. Himpsel, *Nature Communications* **1**, 58 (2010).
 - ²⁵ K. Biedermann, S. Regensburger, T. Fauster, F. J. Himpsel, and S. C. Erwin, *Physical Review B* **85**, 245413 (2012).
 - ²⁶ P. C. Snijders, P. S. Johnson, N. P. Guisinger, S. C. Erwin, and F. J. Himpsel, *New Journal of Physics* **14**, 103004 (2012).
 - ²⁷ G. Kresse and J. Hafner, *Phys. Rev. B* **47**, 558 (1993).
 - ²⁸ G. Kresse and J. Furthmüller, *Phys. Rev. B* **54**, 11169 (1996).
 - ²⁹ P. E. Blochl, *Phys. Rev. B* **50**, 17953 (1994).
 - ³⁰ G. Kresse and D. Joubert, *Physical Review B* **59**, 1758 (1999).

- ³¹ J. S. Shin, K.-D. Ryang, and H. W. Yeom, Physical Review B **85**, 073401 (2012).
- ³² G. Rangarajan and M. Z. Ding, Physical Review E **61**, 4991 (2000).
- ³³ N. D. Mermin and H. Wagner, Physical Review Letters **17**, 1133 (1966).
- ³⁴ S. C. Erwin and C. S. Hellberg, Surface Science **585**, L171 (2005).
- ³⁵ L. W. Bruch, Surface Science **585**, 135 (2005).